2011 American Control Conference
on O'Farrell Street, San Francisco, CA, USA
June 29 - July 01, 2011

Tip-Sample Interaction Force Modeling for AFM Simulation, Control Design, and Material Property Measurement

Sergey Belikov and Sergei Magonov
NT-MDT Development

***Abstract*— Tip-sample interaction force is the key feature measured and manipulated by Atomic Force Microscopy (AFM). It is the main reason why this interaction must be the major component of quasistatic and dynamic controls used in AFM instrumentation. Many dynamic control models are available for AFM but only few explicitly contain the tip-sample forces. One of them is based on asymptotic dynamics using Krylov-Bogoliubov-Mitropolsky (KBM) averaging. In the latter the tip-sample forces acting on approach and retraction are considered. Conservative Hertz model was applied in the first AFM simulations with KMB averaging. This simple and useful model does not cover many aspects of AFM tip-sample interactions (adhesion, energy dissipation, etc.) vital for accurate control of the instrument. The purpose of this paper is to provide adequate interaction force models for AFM control system and illustrate specific features, such as jumping between amplitude branches, adhesive avalanche, etc. These features are routinely observed in AFM experiments but mostly discarded in the control system. We suggest a hybrid model for the control system design to account for these phenomena. The model is based on matching the Maugis's JKR-DMT transition that describes elasto-adhesive interaction after geometrical contact (penetration) and the Integrated Lennard-Jones model with adhesive avalanche that describes the molecular level interaction before the contact. Matching parameters can be calculated based on the assumption that both curves describe the same physical interactions and must match smoothly at the common point of geometrical contact. Hybrid model algorithms are developed that can be used in AFM real-time adaptive control systems with parameter estimation.**

I. INTRODUCTION

Atomic force microscopy (AFM) is the characterization technique for high-resolution visualization of topography and local probing of mechanical and electrical properties of materials. The key of AFM is tip-sample force interactions, and their theoretical description is rather complicated. So far there is no rational match between macroscopic indentation and atomic tip-sample force models that interplay in the experiment due to minute tip-sample separations and contact dimensions. This problem is addressed below, and matching between Maugis JKR-DMT transition and Integrated Lennard-Jones models with adhesive avalanche (LJ-AA) is suggested. We are using Euler-Bernoulli description of the probe dynamics and asymptotic KBM approach to solution of the equation motion of the oscillating probe interacting with a sample [1]. Most of the known treatments of the AFM force spectroscopy studies are based on oversimplified effective point-mass models due to complexity of the problem [2-4]. Asymptotic AFM dynamics [1] with the matching interactive force model described below allows meeting higher AFM quantitative measurement standards.

II. TIP-SAMPLE INTERACTION FORCES IN AFM CONTROL AND MEASUREMENT PROBLEMS

In AFM measurements tip-sample interaction forces are controlled and utilized in every experimental step starting from the tip engagement to a sample. Control of all AFM modes implicitly or explicitly involves the forces and all quantitative measurements are based on deriving parameters of force models from experimental data. Although this topic is extensively covered in literature, only simplified models were applied. In this section we illustrate how tip-sample interaction is used in the control models for dynamic AFM modes (e.g. Amplitude and Frequency Modulation).

Asymptotic equations of AFM dynamic modes near resonance and related analytical classification of the modes were derived and studied in [1]:

$$\begin{cases} \dot{x} = -\dfrac{\varepsilon\omega_1 A_0}{2}\left\{\dfrac{1}{N}\displaystyle\int_0^{\pi}\left[F_a - F_r\right]\left(Z_c + x\cos y\right)\sin y dy + \dfrac{x}{A_0} - \sqrt{1+G^2}\sin\theta\right\} \\ \dot{\theta} = \dfrac{\varepsilon\omega_1 A_0}{2x}\left\{\dfrac{1}{N}\displaystyle\int_0^{\pi}\left[F_a + F_r\right]\left(Z_c + x\cos y\right)\cos y dy + G\dfrac{x}{A_0} + \sqrt{1+G^2}\cos\theta\right\} \end{cases} \quad (1)$$

where the following notations (SI units are shown in brackets) are used: x [m] and θ [rad]-amplitude and phase of the vertical deflection signal; ε[1]-small parameter equal to inverse of quality factor Q; ω_1 [1/sec]-the 1st Eigen-frequency of the cantilever; A_0[m]-the amplitude of free oscillation of the cantilever; N[N]-normalizing force defined at [1, Eq.(26)]; Z_c[m]-central position of the oscillating tip (i.e. height); G[1]-relative frequency shift multiplied by double quality factor; F_a and F_r- the approach and retraction tip-sample forces, whose modeling is the main topic of this work.

Equation (1) describes AFM dynamics for various AFM modes classified in [1]. For example, in Amplitude Modulation (AM) mode G=constant and is typically zero, i.e. cantilever is oscillating at its 1st Eigen-frequency.

In AM spectroscopy mode the tip's central position Z_c is moving up and down with relatively slow (compared to ω_1) speed and two curves are acquired: x vs Z_c (amplitude curve) and θ vs Z_c (phase curve). Typical experimental AFM amplitude and phase curves are shown in Figure 1. The amplitude and phase plots exhibit respectively a kink and a jump from negative to positive values as the amplitude drops ~60% from its initial value. This is a reflection of the bifurcation phenomenon described below.

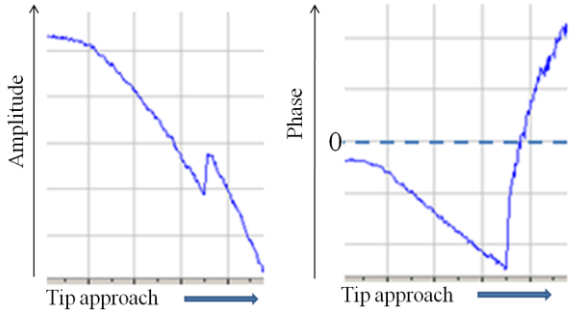

Figure 1. Typical experimental AFM amplitude vs. height (left) and phase vs. height (right) curves. According to the AFM convention the initial phase is defined as zero.

In AM imaging mode tip is scanned horizontally (e.g. by X-Y piezo-scanner) and AFM control system tracks the amplitude set-point $x=A_{sp}$ by moving tip's vertical position Z_c according to the implemented control algorithm. Acquired Z_c vs XY and θ vs XY are displayed as height and phase images.

Height Z_c is usually controlled by piezo-drive and generic dynamics of the drive can be presented in the form

$$H(s, Z_c, u) = 0 \tag{2}$$

where $u=u(x, \theta, Z_c)$ is the control signal e.g. voltage applied to the drive; s is the differential operator. Linearized model of the drive is usually utilized where H is equivalent to the transfer function. X-Y scanning on the sample is either open-loop or use controllers similar to (2). Tip-sample interaction forces depend on X-Y position because of spatial differences of topography and material properties of the sample.

In current AFM controllers, usually PIDs, amplitude-phase dynamics and tip-sample interactions are not explicitly utilized. As a result, tracking of complicated topography profiles and heterogeneous surfaces might be challenging. The resulting AFM curves and images meet only qualitative standards; and there is no model base for true high-resolution imaging and quantitative measurements of material properties of the sample.

An adequate AFM control system design requires a nonlinear model-based approach accounting for tip-sample interaction model with defined and measurable parameters. These parameters vary during XY scan with the spatial changes of local material properties. The latter will be reflected in F_a and F_r behavior, therefore their modeling is crucial for the design. This work provides rigorous derivation of the F_a and F_r based on solid theory and experimental results of many researches assembled in Ref. [5], from LJ-AA molecular interaction (prior to contact) to elasto-adhesion Maugis's JKR-DMT transition (after penetration). These models in combination with AFM dynamics (1), Z-drive and XY dynamics (2) can be used to design AFM control systems that are easier to tune and can meet quantitative measurement standards. Particular control and parameter estimation designs will be presented in further publications.

III. AFM Tip-Sample Interaction Modeling

A. Background

This section provides the basic force interaction models widely used in material science and they are adapted to the purpose of this paper. AFM tip-sample interaction modeling is based on the synergetic match of these models.

1) Integrated Lennard-Jones Potential

Potential per unit area (SI unit [J/m^2]) of attraction between two half-crystals (planes) is [5, p. 31]:

$$U_{PP}(z) = -\frac{4w}{3}\left[\left(\frac{Z_0}{z}\right)^2 - \frac{1}{4}\left(\frac{Z_0}{z}\right)^8\right] \tag{3}$$

where z is the distance between the plates; Z_0 [m] is the equilibrium distance; and w[J/m^2] is the work of adhesion related to Hamaker constant A [J] by the formula

$$w = 2\gamma = A/16\pi Z_0^2$$

2) Derjagin approximation

According to Derjagin approximation [5, formula (1.32)] the interaction force between a sphere of radius R and a plane is

$$F_{RP}(z) = 2\pi R U_{PP}(z) \tag{4}$$[1]

3) Lennard-Jones Model with Adhesive Avalanche (LJ-AA)

Maugis [5, pp 39-45] introduced the dissipative model, called adhesive avalanche, of "two half-crystals rigidly fixed on one edge and having $N/2$ atomic planes free to move". We will reproduce the equations (1.67)-(1.68) of [5] in the form needed for further development of this paper. The main Maugis's idea is to transform D, "rigid interfacial separation", into d, "the interfacial separation when the two half-crystals are elastically deformed by forces acting between them". D is the input distance of the model, and d as function of D substitutes z in formula (3) for the potential. Introducing unit-less quantities:

$$\bar{D} = \frac{D}{Z_0}; \quad \bar{d} = \frac{d}{Z_0}; \quad \bar{z} = \frac{z}{Z_0} \quad \bar{Z}_m = \frac{Z_m}{Z_0} = \sqrt[6]{3} \tag{5}$$

the equations (1.67)-(1.68) of [5] can be written as

$$\begin{cases} \bar{D} = \bar{d} + N\left(\bar{d}\left(\dfrac{2}{\sqrt{4\bar{d}^6 - 3} - 1}\right)^{1/3} - 1\right), & \text{if } \bar{d} > \bar{Z}_m \\ \bar{D} = \bar{d} + N(\bar{d} - 1), & \text{if } \bar{d} \le \bar{Z}_m \end{cases} \tag{6}$$

Figure 2 plots D/Z_0 vs. d/Z_0 defined by equation (6) for different N. Solution

$$\bar{z} = \bar{d}(\bar{D}; N) \tag{7}$$

of equation (6) may have several branches, as illustrated in Figure 2, that, when substituted to (3), adds hysteresis to the potential and related force model (4). We will use parameters N and Z_0 to match with the elasto-adhesive models described in the next subsection. Solution for D=0

$$\bar{d}(0, N) = N/(N+1) \tag{8}$$

[1] Formula in [5] has sign "-" for the force directed to the plate (down). In AFM convention, force is directed up; for interaction of two spheres with radii R_1 and R_2, $R=0.5R_1R_2/(R_1+R_2)$.

will be used below.

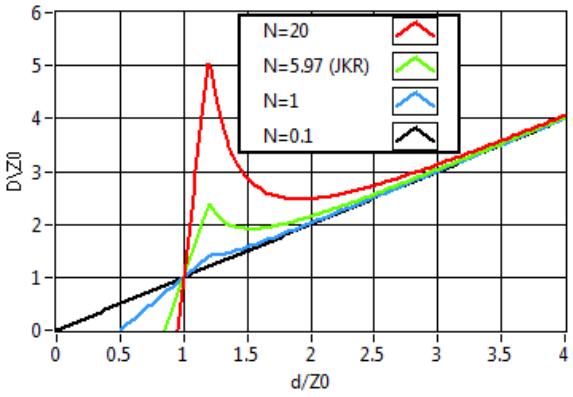

Figure 2. Plot of D/Z_0 vs. d/Z_0 defined by equation (6)

4) Elasto-Adhesive models (Maugis's JKR-DMT transition)

In this subsection formulas are summarized for the case of the frictionless contact of a sphere of radius R and a half-space (or two spheres –see footnote [1]). The following notations are used (SI units are shown in brackets): a[m]-radius of contact; K[Pa]=(4/3)E^*, where E^*[Pa] is reduced elastic modulus; P[N]-interaction force; h[m]-penetration of the sphere into the half-plane.

Using unit-less quantities (formulas (4.200-4.202) in Ref. [5]):

$$A=\frac{a}{\left(\pi w R^2/K\right)^{1/3}};\quad \overline{P}=\frac{P}{\pi w R};\quad \overline{\Delta}=\frac{h}{\left(\pi^2 w^2 R/K^2\right)^{1/3}} \tag{9}$$

Maugis's λ-parametric elasto-adhesive model that connects JKR and DMT is the following [5, formulas 4.204-4.206]

$$\overline{P}=A^3-\lambda A^2\left(\sqrt{m^2-1}+m^2\tan^{-1}\left(\sqrt{m^2-1}\right)\right) \tag{10}$$

$$\overline{\Delta}=A^2-\frac{4}{3}A\lambda\sqrt{m^2-1} \tag{11}$$

$$\frac{\lambda A^2}{2}\left[\sqrt{m^2-1}+\left(m^2-2\right)\tan^{-1}\sqrt{m^2-1}\right]+\frac{4\lambda^2 A}{3}\left[\sqrt{m^2-1}\tan^{-1}\sqrt{m^2-1}-m+1\right]=1 \tag{12}$$

Equations (10)-(12), after excluding A and m, describe relationship $\overline{P}=\overline{P}\left(\overline{\Delta};\lambda\right)$ between force and penetration with the Maugis parameter λ. This parameter describes transition [5, p. 290] between JKR (as $\lambda\to\infty$)

$$A^3=\overline{P}+A\sqrt{6A};\quad \overline{\Delta}=A^2-\frac{2}{3}\sqrt{6A} \tag{13}$$

and DMT (as $\lambda\to 0$)

$$A^3=\overline{P}+2;\quad \overline{\Delta}=A^2 \tag{14}$$

This λ-parametric model will be used to match with LJ-AA model in Section III C.

B. *Bifurcations due to cantilever spring constant in frame of Integrated Lennard-Jones model*

In AFM as well as other devices measuring deflection of the cantilever, the deflection ($z-Z_c$) due to tip-sample interaction is determined by the force balance. In the case of Integrated Lennard-Jones model (3) with Derjagin approximation (4), the force balance is

$$F(z,Z_c)=F_{RP}(z)-k(z-Z_c)=0 \tag{15}$$

where k [N/m] is the cantilever spring constant.

Depending on Z_c, solutions of equation (15) may have several branches, stable and unstable. Condition of stability is $\partial F/\partial z<0$, and positions where

$$\frac{\partial F}{\partial z}=\frac{16\pi R w}{3Z_0}\left[\left(\frac{Z_0}{z}\right)^3-\left(\frac{Z_0}{z}\right)^9\right]-k=0 \tag{16}$$

are bifurcation points. These bifurcations change the force interactions by adding hysteresis as shown in Figure 3.

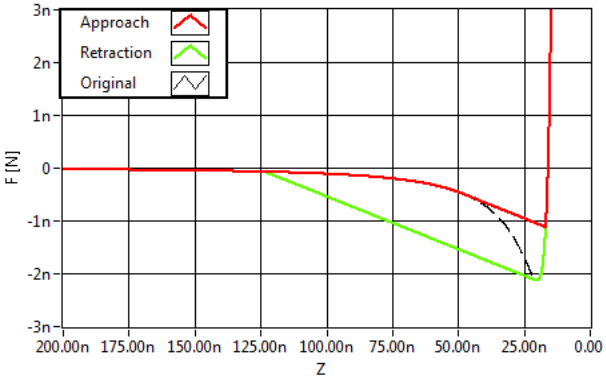

Figure 3. Integrated Lennard-Jones tip-sample interaction: tip radius R=10nm; work of adhesion w=34mJ/m^2; Integrated Lennard-Jones equilibrium distance Z_0=20nm; cantilever spring constant k=20mN/m.

Values of z (horizontal axis on the plot) are increasing from right to left. To match with elastic solid models (where penetration is positive) distance from contact should be negative by convention. See formula (17) below.

Equation (16) also provides the upper limit on spring constant k for existence of these bifurcations. LHS of (16) is a third order polynomial on $y=(Z_0/z)^3$. Thus, condition of existence of bifurcations is that the equation

$$y^3-y+\frac{3kZ_0}{16\pi R w}=0$$

has two positive roots which is the case if

$$k<\frac{32\pi R w}{9\sqrt{3}Z_0}$$

This can be verified from the equivalent condition that local minimum of the polynomial is negative (from derivative, local minimum is at $y=3^{-1/2}$). For numerical values of Figure 2, k is less than 109.634 [mN/m].

Illustrated on Integrated Lennard-Jones model, these bifurcations (based on stability change of force equilibrium described by (15), (16)) are applicable to any force model as illustrated below in Figure 5 (green arrows) for LJ-AA—JKR-DMT matching.

Figure 4 shows the simulated amplitude curve branches for the parameters of Figure 3. The calculation procedure was

implemented using the system described by Equation (1). Two stable branches are well known to AFM practitioners as low- and high amplitude branches. The jump from low to high amplitude branch is visible as the kink in the experimental curve shown in Figure 1. It is important to be able to select the branch that better suits an experiment. For example, it is clear from Figure 4 that high-amplitude branch (red) would not be a good choice because it is close to the unstable branch (black) and is difficult for tracking. In other situations jump (avalanche) from low- to high- amplitude branch may occur for much larger height and only the high-amplitude branch is available for operations. AFM control system with parameter estimator is able to select the optimal branch for operations.

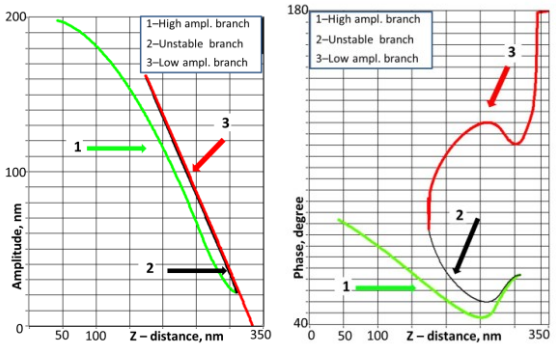

Figure 4. Simulated amplitude and phase curves for the tip-sample interaction of Figure 3. Free amplitude A_{free}=199 nm

C. *Matching Maugis JKR-DMT Transition and LJ-AA Models*

The matching Maugis JKR-DMT Transition (9)-(12) that describes elasto-adhesive interaction after geometrical contact (penetration), and Lennard-Jones model with adhesive avalanche (LJ-AA) that describes the molecular level interaction before the contact, was suggested in [1, section IV] and is implemented below. All calculations and simulations described in [1, 6] were based on simple Hertz model. The model matching described below for spherical tip and plane sample (or spherical sample –see footnote [1]) covers major aspects for this type of interactions. It can be similarly extended to other types, e.g. by using Ref. [7] that describes models that extends JKR, DMT and Maugis's transition for arbitrary axi-symmetrical tip shape and Ref. [8] that covers analytics of van der Waals forces for major practical situations.

Figure 5 shows the principle of matching. Left part of the Figure shows series of force curves described by equations (4)-(7) with parameters (N, Z_0) and right part –series of curves described by equations (9)-(12) with parameter λ. All curves are plotted in unit-less coordinates $\overline{P}$ vs. $\overline{\Delta}$ defined in (5). In Figure 5, $\overline{\Delta}$ is positive for the right part (Elastic solid) and negative for the left part (Lennard-Jones solid). To distinguish the curves, we use notation $\overline{F}$ for the Lennard-Jones and $\overline{P}$ for Elastic solid. We also use notation $\overline{\Delta}_{LJ} \le 0$ for the horizontal coordinate of the Lenard-Jones solid (according to convention described in Figure 3) so that the series of curves are:

$$\overline{F}\left(\overline{\Delta}_{LJ}; Z_0, N\right),\ \overline{\Delta}_{LJ} \le 0;\ N \ge 0 \qquad (17)$$

and

$$\overline{P}\left(\overline{\Delta}; \lambda\right),\ \overline{\Delta} \ge 0;\ \lambda \ge 0 \qquad (18)$$

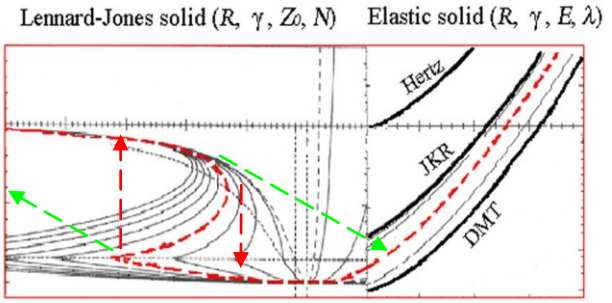

Figure 5. Match of Lennard-Jones with adhesive avalanche (LJ-AA) and elastic solid models (JKR-DMT transition) by fitting parameter N and P_0. Red arrows show jumps "to contact" (down) during the approach and "from contact" (up) during the retraction. Green arrows show bifurcations due to soft cantilever similar to those in Fig. 3.

The relationship between $\overline{D} \ge 0$ in (5)-(7) and $\overline{\Delta}_{LJ} \le 0$ in (17) follows from their definitions:

$$\overline{D} = -\frac{\overline{\Delta}_{LJ}\left(\pi^2 w^2 R / K^2\right)^{1/3}}{Z_0} \qquad (19)$$

Each parameter λ in (18) defines the curve and the value

$$\overline{P}_0 = \overline{P}\left(0; \lambda\right) \qquad (20)$$

Equation (20) is one-to-one relationship between $\overline{P}_0 \in \left[-2, -4/3\right]$ and $\lambda \in \left[0, \infty\right]$, where the left end defines DMT curve and the right –JKR curve. This allows to select $\overline{P}_0$ as the curve parameter instead of λ. This parameter has clear physical meaning –the normalized value of the curve at zero-penetration. Another advantage of using $\overline{P}_0$ is that it can be extended beyond JKR-DMT transition (to the curves that are above the JKR with $\overline{P}_0 > -4/3$ in Figure 5). So, instead of (18) we will use the series of curves

$$\overline{P}\left(\overline{\Delta}; \overline{P}_0\right),\ \overline{\Delta} \ge 0;\ \overline{P}_0 \ge -2 \qquad (21)$$

with $\overline{P}_0 = -2$ for DMT, $\overline{P}_0 = -4/3$ for JKR and reserve for $\overline{P}_0 > -4/3$. Authors are not aware about any theoretical development of these reserve curves but observed them in AFM experiments.

Parameters R (radius of the tip), K (value proportional to the reduced elastic modulus), w (work of adhesion), and $\overline{P}_0$ are geometrical and material properties that can be quantitatively measured[2] and assumed to be fixed[3].

[2] Model-based quantitative nanomechanical measurements with AFM are described in [7, 11].

[3] However, these parameters may be unknown and require estimators in adaptive control systems

From the other hand, parameters N and Z_0 are not directly measurable. These parameters can be calculated based on the assumption that left (Lennard-Jones) and right (elastic) curves describe the same physical system and as a consequence must match smoothly at the common point $\overline{\Delta} = \overline{\Delta}_{LJ} = 0$. This leads to the following equations for the parameter N

$$\overline{P}\left(0;\overline{P}_0\right) = \overline{P}_0 = \overline{F}\left(0;N\right) \qquad (22)^4$$

and, after finding N, the equation for parameter Z_0,

$$\left.\frac{\partial \overline{P}\left(\overline{\Delta};\overline{P}_0\right)}{\partial \overline{\Delta}}\right|_{\overline{\Delta}=0} = \left.\frac{\partial \overline{F}\left(\overline{\Delta}_{LJ};Z_0,N\right)}{\partial \overline{\Delta}_{LJ}}\right|_{\overline{\Delta}_{LJ}=0} \qquad (23)$$

$$= \left.\frac{\partial \overline{F}\left(\overline{D};N\right)}{\partial \overline{D}}\right|_{\overline{D}=0} \left[-\left(\pi^2 w^2 R/K^2\right)^{1/3}\right]\frac{1}{Z_0}$$

or

$$Z_0 = \left(\pi^2 w^2 R/K^2\right)^{1/3} \overline{Z}_0\left(\overline{P}_0\right) \qquad (24)$$

where

$$\overline{Z}_0\left(\overline{P}_0\right) = -\frac{\left.\frac{\partial \overline{F}\left(\overline{D};N\left(\overline{P}_0\right)\right)}{\partial \overline{D}}\right|_{\overline{D}=0}}{\left.\frac{\partial \overline{P}\left(\overline{\Delta};\overline{P}_0\right)}{\partial \overline{\Delta}}\right|_{\overline{\Delta}=0}} \qquad (25)$$

and $N\left(\overline{P}_0\right)$ is the solution of equation (22).

We now discuss computational procedures of finding N and Z_0 from equations (22) and (24), (25).

According to (8), for $\overline{D} = 0$,

$$\overline{z} = \overline{d} = N/\left(N+1\right) \qquad (26)$$

Substituting this to (4), using (5) and (9), obtain

$$\overline{F}\left(0;N\right) = \frac{1}{\pi w R} F_{RP}\left(z\right) = \frac{8}{3}\left[\frac{1}{4}\left(\frac{1}{\overline{z}}\right)^8 - \left(\frac{1}{\overline{z}}\right)^2\right] \qquad (27)$$

$$= \frac{1}{3}\left[2x^4 - 8x\right], \text{ where } x = \left(\frac{N+1}{N}\right)^2$$

Then the solution of equation (22) is

$$N = \left(\sqrt{x} - 1\right)^{-1} \qquad (28)$$

where x is a root of the polynomial equation

$$2x^4 - 8x - 3\overline{P}_0 = 0, \quad x > 1 \qquad (29)$$

Table 1 describes the regions of parameter $\overline{P}_0$ and corresponding ranges of N (solution of equation (22)) and λ. The Table and Figure 5 demonstrate that Lennard-Jones solid with adhesive avalanche (LJ-AA) covers the whole ranges of $\overline{P}_0$ and N, while there is a gap for $\overline{P}_0 > -4/3$, $N < 5.97$, (λ→∞ with $\overline{P}_0 \to -4/3$ making JKR a limiting case) where no theoretical model of interaction after penetration is available for $\overline{P}_0 > -4/3$. This must be filled because the curves from the gap do occur in AFM experiments.

[4] At zero, $\overline{F}\left(0;Z_0,N\right)$ of (17) does not depend on Z_0

$\overline{P}_0$	N	λ	Comments
-2	∞	0	DMT after penetration –long-range constant attractive force before the contact
(-2, -4/3)	(∞, 5.97)	(0,∞)	Maugis's DMT-JKR transition –LJ-AA
-4/3	5.97	∞	JKR –LJ-AA with N=5.97
(-4/3,∞)	(5.97, 0)	na	No model available after penetration –LJ-AA before the contact
∞	0	na	Classical Lennard-Jones force (no adhesive avalanche) goes to infinity approaching the sample – penetration is not possible

Table 1. Ranges of parameter $\overline{P}_0$, corresponding λ and N –solution of (22); (22) can be found by algorithm (28)-(29).

After matching N is found, Z_0 can be calculated by formula (24) to make the transition smooth. Z_0 depends on geometry (R), material properties (w, K) and, according to formula (25), on derivatives of well defined functions at zero with a given parameter $\overline{P}_0$. Calculations of the derivatives may be time consuming for real-time operations. In this case the unit-less function $\overline{Z}_0\left(\overline{P}_0\right)$ can be tabulated, e.g. for the range of $\overline{P}_0 \in \left[-2,-4/3\right]$ to be used for the curves described by DMT-JKR transition.

IV. Experimental Cases

Figure 6A-C shows amplitude vs. distance and force vs. distance curves, which were recorded on polystyrene (PS) with three Si probes having different stiffness 40N/m, 4N/m and 0.4N/m. Initially, the probes were oscillating with the amplitude of ~30 nm that decreases to zero and the tip and sample come into intermittent contact. On further sample excursion the damped probes deflected due to strong repulsive interactions. The force curves recorded with the stiffer probe does a moderate attractive interaction and a non-linear repulsive part that indicates on elastic deformation of the sample. Such curves can be used for calculation of elastic modulus of polymer materials as shown in Ref. [7,11]. The adhesion effect is best detected in the force curves recorded with softest probe, Figure 6C. The linear repulsive force response indicates that this probe is not stiff enough for making indentation. On approach, the soft probe snaps into the surface when the attractive force gradient becomes larger than probe stiffness. The pull-out force is stronger on the probe retraction from the surface. The amplitude curve recorded with the probe of intermediate stiffness exhibits a kink common to the bifurcation effect. At the same time the probe exercises the attractive interaction that followed by small snap into contact. The retraction trace is only slight different from the approach one. This case study reveals that a most sensitive detection of the tip-induced indentation and adhesive effects might require the use of a particular probe. This does not mean that adhesion can be disregarded in the analysis of the indentation results.

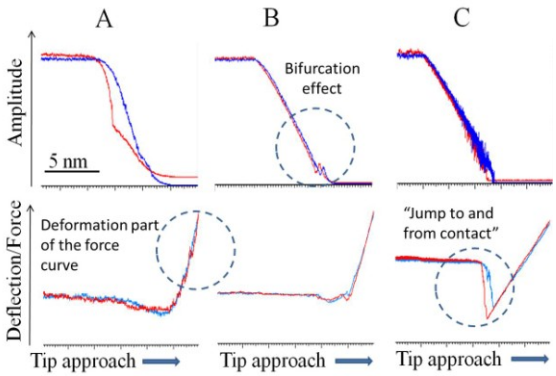

Figure 6. Amplitude and force curves obtained on polystyrene films using Si probes with stiffness 40 N/m (A), 4 N/m (B) and 0.4 N/m (C). The blue and red traces correspond to the probe approach and retraction. The amplitude and deflection axis is in arbitrary units.

It is worth noting that these force curves were obtained at relatively low frequencies, e.g. one approach-retraction cycle per second. In oscillatory modes, where either an amplitude damping or a frequency change are employed for monitoring the tip-sample force interactions, the approach-retract cycle is in the 50-400 kHz range. The recording of the force curve during the fast cycle is challenging but already feasible with the use of specially-shaped probes [9-10]. The analysis of these curves, (currently limited to repulsive part of the approach curve using Hertz, JKR or DMT models [7,11]) will meet better quantitative standards by using JKR-DMT - LJ-AA matching model applied to repulsive and attractive regions of both approach and retraction experimental curves. Viscoelastic nature of polymers results in frequency dependence of their mechanical properties that is not considered by the above models. Further theoretical and experimental work is needed in this respect.

V. Control, Simulation and Measurement Strategy

AFM asymptotic dynamics (1) with states (x, θ) = (amplitude, phase) along with the JKR-DMT—LJ-AA matching model for F_a and F_r can be used for advanced control of the AFM experiment, simulation of the images and force curves, and local measurements of materials properties. Practical system designs for these applications will be described in forthcoming publications while some short notes are presented here.

Control. Both experimental (Fig. 1) and simulated (Fig. 2) amplitude/phase curves indicate that the control system (1) is a hybrid system with three discrete states: Low Amplitude; High Amplitude; and Bifurcation. Formally there is also the fourth state corresponding to the unstable branch in Figure 4. AFM control system tracking the set-point amplitude should identify and select a discrete state and avoid jump to another state (through bifurcation). This can be achieved by real-time parameter estimation and adaptive tracking of the state based on the estimated parameters. When the discrete state is selected, many of available adaptive control techniques with parameter estimation are applicable.

Stable tracking of the set-point amplitude is the key feature of the precise profiling of the complex surface structures with minimal tip wear. Knowledge about tip-sample forces is also invaluable for choosing scanning conditions with a minimal contact area (that can be calculated from the parametric force model) leading to high-resolution imaging.

Using the model and the discrete state, amplitude set-point can be paired with the phase set-point (as in Figure 4). Then system (1) can be linearized near this set-point pair and linear control design with parameter adaptation can be utilized.

Simulation. Reference [6] describes an AFM simulator based on Hertz model. Implementing the JKR-DMT—LJ-AA matching described in this paper allows simulation of much more complicated and realistic AFM experiments. This is also true for simulation of frequency modulation mode experiments that are performed in different environments.

Measurement. Outputs of parameter estimator used in adaptive control can be used for real-time material properties mapping. Another and more accurate interactive analysis can be based on off-line fitting of experimental force curves. Successful quantitative AFM measurements based on JKR model were reported in Refs. [7,11] and will benefit from using matching model described in this paper to measure more complicated "non-JKR" materials. The model matching technique can be extended to other forces sensed prior the tip-sample contact, e.g. electrostatic.

At this time the described matching models are under experimental verification. Of particular interest are the cases where electrostatic tip-sample interactions are enhanced by using the conducting probes and measurements are performed in different humidity. In the latter practically-important case a meniscus force becomes the additional constituent of the overall tip-sample force interactions.

Results of verification and use of the model will be topics for forthcoming publications.

VI. Summary

The hybrid model of tip-sample force interactions that includes macroscopic deformation and atomic force potential with adhesive avalanche is a substantial step in extending the control of AFM measurements and simulation of AFM experiments for more realistic non-conservative cases. A rational theoretical description of tip-sample forces needs to address the local measurements of electrostatic forces that represent a fast increasing part of AFM applications.

References

[1] S. Belikov, S. Magonov, Proceed. *Am. Control Conf.* 2009, 979.
[2] B. Capella and G. Dietler, *Surf. Sci. Rep.* 1999, *34*, 1.
[3] R. Garcia, and R. Perez, *Surf. Sci. Rep.* 2002, *47*, 197.
[4] X. Xu, J. Mecher, and A. Raman, *Phys. Rev. B* 2010, *81*, 035407.
[5] D. Maugis, *Contact, Adhesion and Rapture of Elastic Solids*, Springer, 2000.
[6] S. Belikov, S. Magonov, Proceed. *Am. Control Conf.* 2010, 5745.
[7] S. Belikov et al, *JVST B* 2009, *27*(2), 984.
[8]V. A. Parsegian, *Van der Waals Forces*, Cambridge Univ. Press, 2006.
[9] O. Sahin, et. al. *Nature Nanotechnol.* 2007, *2*, 507.
[10] A. Sarioglu, and O. Solgard, *Appl. Phys. Lett.* 2008,*93*, 023114.
[11] H. Lakrout et. al., *Proceed. Adhesion Soc. Meeting*, 2008.